

Catalytic Upgrading of Pyrolysis Bio-oil by Hydrotreating and Emissions Estimation of Combustion of Gas-phase Compounds

Rami Doukeh

Petroleum & Gas University of Ploiești

Dorin Bombos

Petroleum & Gas University of Ploiești

Mihaela Bombos

National Institute for Research and Development for Chemistry and Petrochemistry ICECHIM Bucuresti

Elena-Emilia Oprescu

Petroleum & Gas University of Ploiești

Gheorghe Dumitrascu

Gheorghe Asachi Technical University of Iași

Gabriel Vasilevici

National Institute for Research and Development for Chemistry and Petrochemistry ICECHIM Bucuresti

Catalina Calin (✉ catalina.calin20@yahoo.com)

Chemistry Department, Petroleum-Gas University of Ploiesti, 39 Bucuresti Blvd., 100680, Ploiesti, Romania

Research Article

Keywords: Hydrotreating, pyrolysisbio-oil, catalyst, biofuel, upgrading

Posted Date: December 15th, 2020

DOI: <https://doi.org/10.21203/rs.3.rs-121272/v1>

License: © ⓘ This work is licensed under a Creative Commons Attribution 4.0 International License.

[Read Full License](#)

Version of Record: A version of this preprint was published at Scientific Reports on March 17th, 2021. See the published version at <https://doi.org/10.1038/s41598-021-85244-z>.

Catalytic upgrading of pyrolysis bio-oil by hydrotreating and emissions estimation of combustion of gas-phase compounds

Rami Doukeh¹, Dorin Bombos¹, Mihaela Bombos², Elena-Emilia Oprescu^{1,2*}, Gheorghe Dumitrascu³, Vasilievici Gabriel², Catalina Calin^{1*}

¹Chemistry Department, Petroleum-Gas University of Ploiesti, 39 Bucuresti Blvd., 100680, Ploiesti, Romania

²National Institute for Research and Development for Chemistry and Petrochemistry ICECHIM Bucuresti, 202 Splaiul Independentei, 060021, Bucharest, Romania

³Department of Engineering Thermodynamics, “Gh. Asachi” Technical University of Iasi, Bd. D. Mangeron, 59-61,6600 Iasi, Romania

Correspondence to: catalina.calin20@yahoo.com; catalina.calin@upg-ploiesti.ro; oprescuemilia@gmail.com

Abstract:

An attractive solution for improvement of pyrolysis bio-oil composition regarding the high content of oxygenated compounds is catalytic upgrading via hydrotreating process. The objective of this work is to evaluate the catalytic activity of CoMo / γ -Al₂O₃-HMS in bio-oil hydrotreating. The catalyst was characterized by surface area, X-ray diffraction (XRD), TEM, FT-IR and XPS analysis. The experiments were carried out in a flow fixed-bed reactor at the temperature range of 250-320 °C, pressure between 20-40 bar, and LHSV 3h⁻¹. The results showed that increased temperature and pressure favors the hydrodeoxygenation process, reaching the maxim bio-oil conversion of 87.23%. Also, a chemical modelling algorithm was developed in order to evaluate the harmful emissions resulted from hydrotreating gaseous phase combustion. This calculation algorithm can be applied to any pressurized or atmospheric combustion engine fueled with different mixture of combustible gases such as: natural gas, hydrogen-enriched natural gas and oxy-fuel.

Keywords: Hydrotreating, pyrolysisbio-oil, catalyst, biofuel, upgrading

Introduction

Biogas plants are alternative sources for renewable energy, biomass waste treatment and organic fertilizers (digestion waste, i.e. digestate). However, an accumulation of biogas plants in certain regions might lead to an oversupply of digestate [1], causing many environmental concerns (odor control, transportation cost, pathogen, heavy metal (loid) contamination) [2]. Digestate pyrolysis can be an environmentally and energy recovery solution for digestate disposal [3]. Typically, this process is performed between 400 and 700°C at near atmospheric pressure or below, in the absence of oxygen. Bio-oil produced from biomass pyrolysis has the potential to become an alternative renewable fuel and raw material for fine chemicals production generating thus bio-based high added value products [4].

In general, pyrolysis oil contains hundreds of organic compounds including hydrocarbons and oxygenated compounds (i.e. organic acids, aldehydes, ketones and phenolics) [5] which cause bio-oil to have low heating value, low solubility in commercial hydrocarbons, poor thermal and chemical stability and high acidity, high viscosity and high corrosiveness than petroleum [6,7]. However, pyrolysis oil can be converted to transportation fuel by catalytic treatment. The catalysts and conditions used are very similar to those used in petroleum hydrodesulfurization, hydrotreating, and hydrocracking processes, more generally described as hydroprocessing. [8] A promising upgrading technology is considered to be catalytic hydrotreatment of bio-oil, which involves treatment of pyrolysis oil with hydrogen in the presence of a heterogeneous catalyst leading to gasoline or diesel like products [9].

Different hydrotreating catalysts have been investigated, such as NiMo and CoMo sulfides, Ni/SiO₂, Ni/ZrO₂, Ni/CeO₂, Ni/Al₂O₃, Ni-Cu/SiO₂, Ru/C, Pt/C, Pd/C, Pd/SiO₂, Pt-Ni/SiO₂, Pd-Ni/SiO₂ and Cu/SBA-15 [10]. Among these, NiMo and CoMo sulfides catalyst have been widely used in bio-oil hydrotreating. However, the main disadvantage of these catalysts is the requirement of the presence of sulphur to remain active. Furthermore, deactivation of the catalysts as a function of time on stream was reported [9]. Wildschut J. et al., [11] compared the results of typical hydrotreatment catalysts (sulfide NiMo/Al₂O₃ and CoMo/Al₂O₃) with heterogeneous noble-metal catalysts (Ru/C, Ru/TiO₂, Ru/Al₂O₃, Pt/C, and Pd/C). The Ru/C catalyst was found to be superior to the classical hydrotreating catalysts with respect to oil yield (up to 60 wt %) and deoxygenation level (up to 90 wt %). However, due to the high cost and low availability of noble metals, their industrial applications become more difficult [12]. In other reports [13,14], better results compared with Ru/C and MoP/C concerning oxygen content and bio-oil yield were obtained when transition metal phosphides, such as Ni₂P and MoP, have been tested.

In recent years, non-noble metal catalysts based on less-expensive nickel metals have been reported to exhibit high activity for decarboxylation/decarbonylation process [15]. Ardiyanti et al., [16] studied the hydrotreatment of pyrolysis oil over Ni-Cu catalysts on various supports (CeO₂-ZrO₂, ZrO₂, SiO₂, TiO₂, rice husk carbon (CRH), and Sibunit). The Ni-Cu/TiO₂ catalyst shows the best performance in catalytic hydrotreatment of fast pyrolysis oil. Moreover, molybdenum-doped Ni-based catalysts can enhance the activity of methanation, reinforce sulfur resistance and heat resistance of the catalysts, simultaneously [17, 15]. In order to study the effect of Cu and Mo loading on Ni/ γ -Al₂O₃ catalytic performance, Jing Zhong-yu et al [15] prepared and tested a series of Ni/ γ -Al₂O₃ catalysts with or without Cu and Mo components. The results suggested that Cu and Mo modified catalysts demonstrate better catalytic performance than Ni/ γ -Al₂O₃ catalysts due to the combining effect of Cu which is a very effective promoter of Ni for the decarboxylation/decarbonylation, meanwhile, Mo promotes the hydrodeoxygenation [15]. Therefore, in this work one catalyst based on CoMo / γ -Al₂O₃-HMS was prepared and tested on hydrotreatment of digestat pyrolysis oil. The influence of temperature and pressure on bio-oil composition and deoxygenation efficiency was investigated in terms of. Also, the main combustion noxious emissions, i.e. CO₂, CO and NO_x, for the gaseous mixture fuel resulted during hydrotreating process were evaluated through a combustion chemistry model.

Results and discussion

Catalyst characterization

The textural properties, such as specific surface area, pore size distribution and pore volume of the γ -Al₂O₃-HMS support and corresponding CoMo catalyst, were evaluated by nitrogen adsorption-desorption isotherms, and these characteristics are presented in Table 1. The γ -Al₂O₃-HMS support has a high specific surface area of 308.37 m²/g, a mean pore diameter of 5.49 nm and a total pore volume of 0.631 cm³/g. The addition of Co and Mo to γ -Al₂O₃-HMS support leads to a decrease in textural properties. The pore size and pore volume reflect a decrease of about 30% after impregnation indicating that impregnation may block the pores (Table 1).

Table 1. Textural properties of the support and of the catalyst

Sample	Surface area (m ² /g)	Pore volume (cc/g)	Mean pore diameter Dv(d) (nm)
γ -Al ₂ O ₃ -HMS	308.37	0.631	5.49
CoMo/ γ -Al ₂ O ₃ -HMS	280	0.440	3.66

The N₂ adsorption-desorption isotherm of the support and its catalyst is attributed to IV type isotherm (Figure 1 and 2) and the nitrogen isotherm reveals a hysteresis loop of H2 and H3-type respectively. The alteration of hysteresis loop shape for CoMo/ γ -Al₂O₃-HMS catalyst also indicate that there is plugging of mesopores and there are changes in the support structure after impregnation.

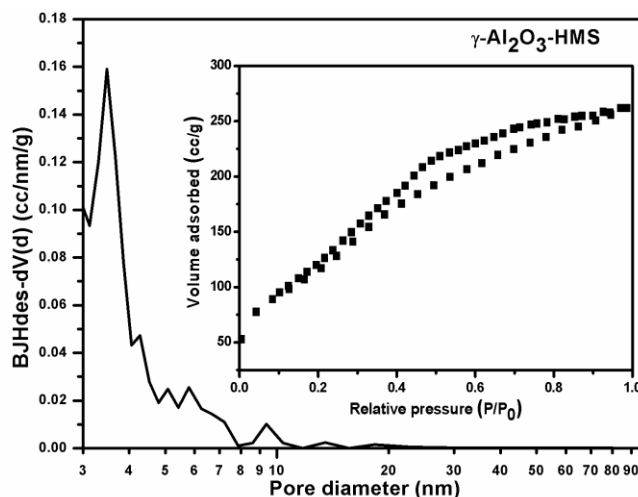


Figure 1. Pore size distribution and adsorption-desorption isotherm of the γ -Al₂O₃ –HMS support

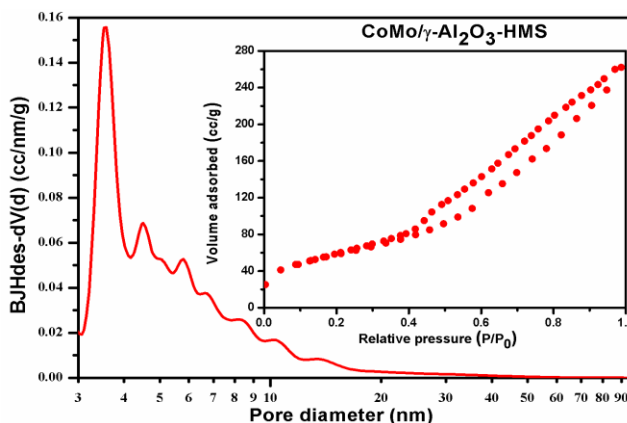


Figure 2. Pore size distribution and adsorption-desorption isotherm of the CoMo/ γ -Al₂O₃ –HMS catalyst

SEM images of the synthesized CoMo/ γ -Al₂O₃-HMS catalyst are shown in Figure 3 with different magnifications (the left-side image scale bar is 100 μ m and the right-side 5 μ m) and show the homogeneity of the sample.

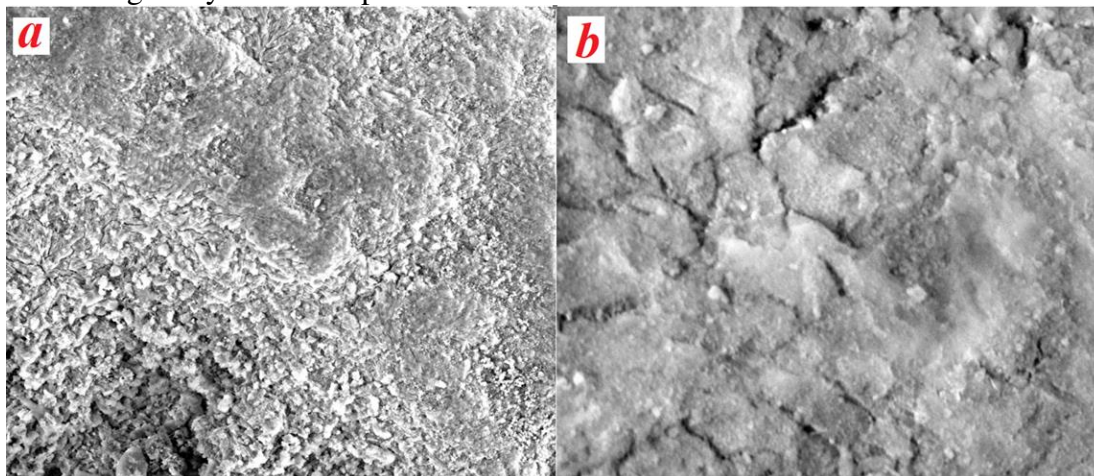


Figure 3. SEM images of the catalyst CoMo/ γ -Al₂O₃-HMS **a)**100 μ m and **b)** 5 μ m image scale bar

The FTIR spectrum of the catalyst (Figure 4) shows broad bands around 3420 cm^{-1} and 1630 cm^{-1} , which were assigned to stretching and bending modes of –OH groups. The peaks in the region of 450-800 cm^{-1} were assigned to the oxide structures. The accurate assignment of the bands to specific compounds was difficult because the different compound bands overlap. The Si-O-Si specific bands (from HMS) are assigned at 1090 cm^{-1} , 950 and 800 cm^{-1} [18].

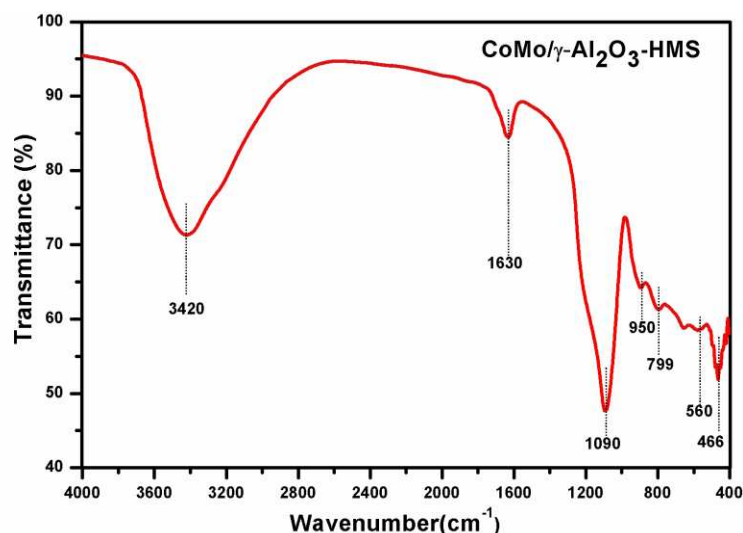


Figure 4. IR spectrum of CoMo/ γ -Al₂O₃-HMS catalyst

The surface components and chemical states of metal species on the catalysts were studied by XPS survey spectra. Results obtained by this technique are shown in Figure 5 and

Table 2. XPS signals were assigned according to the literature and the official web page of National Institute of Standards and Technology (NIST)[19]. Binding energies in the ranges of 780–783 eV and 232 eV are ascribed to Co2p and Mo3d spectra and 154eV to Si 2s. The characteristic Mo 3d_{5/2} peak at 232.12 eV indicate the presence of Mo⁶⁺ which can be attributed to MoO₃ [20,21]. Co is present as Co³⁺ and Co²⁺ species. The binding energy of Co³⁺, with the Co 2p_{3/2} profile, is 782.27 eV which could be ascribed to Co₃O₄ and CoOOH [22,23] Co²⁺ may be present as CoO and CoAl₂O₄ [24] with Co 2p_{3/2} peak at 780.68 eV. From the calcination step of the catalyst preparation it could also be formed Co and Mo aluminates or double oxides containing Co and Mo. According to figure 6 and Table 2, Si (from HMS mesoporous silica) occurs in the Si 2s energy range of 154.23 eV, assigned to Si⁴⁺ (SiO₂).

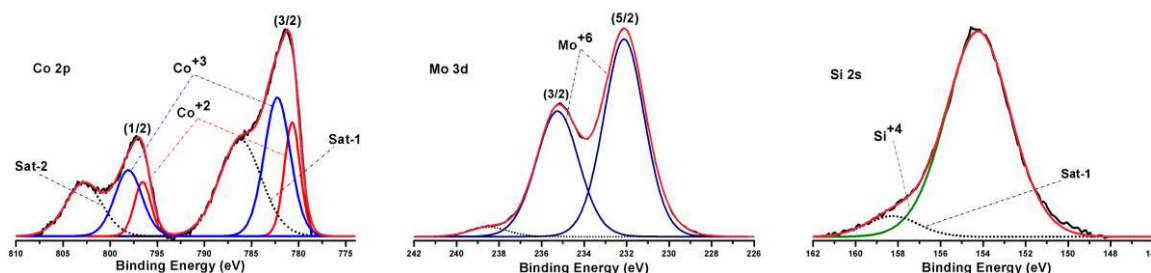


Figure 5. XPS Co 2p, Mo 3d and Si 2s spectra of CoMo/ γ -Al₂O₃-HMS catalyst

Table 2. XPS binding energies and assigned species for Co 2p, Mo 3d and Si 2s

Element	Spectral line	Energy (eV)	Assigned species
Co	2p _{3/2}	782.27	Co ⁺³
	2p _{3/2}	780.68	Co ⁺²
Mo	3d _{5/2}	232.12	Mo ⁺⁶
Si	2s	154.23	Si ⁴⁺

Chemical composition of pyrolysis bio-oil

The chemical composition of pyrolysis bio-oil is shown in Fig. 1S. Chromatogram analysis reveals the presence of a large number of components. The main compounds identified were unsaturated organic compounds, carbonyl compounds, furan derivatives, phenols, lower carboxylic acids and unsaturated fatty acids. These compounds have a different polarity and a wide range of boiling point. Compounds with high reactivity containing olefin groups conjugated with carbonyl groups (i.e. cyclopenten-1-one derivatives) were also been identified. These compounds can deactivate the catalyst at high temperatures due to the formation of oligomers.

The physical characteristics of the pyrolysis bio-oil (Table 3) show a relatively high water content (over 25 w.t %), a density about 0.9956 g / mL due to the presence of water and lower carboxylic acids (acetic, propionic and butyric) in relatively high concentrations. The presence of lower carboxylic acids and fatty acids justifies the high total acid number and saponification number of almost 135 and respectively, 224.12 mg KOH /g.

Table 3. The physical characteristics of the pyrolysis bio-oil

Property	Value	UM
Density	0.9956	g/mL
Water content	25.10	%
Total acid number	134.9	mg KOH/g
Saponification number	224.12	mg KOH/g

Catalysts activity evaluation

The catalytic activity of CoMo / γ -Al₂O₃-HMS for the bio-oil hydrotreating was evaluated in the temperature range of 250-320°C, pressure between 20-40 bar, and constant LHSV of 3h⁻¹.

The effect of temperature over bio-oil yield is presented in figure 6. The results showed that the bio-oil conversion increases gradually with temperatures, from 62.86 % to over 77.42 % at maxim temperature of 320°C. This behavior is due to the different reactivity of the various classes of oxygenated compounds present in the bio-oil. The phenolic as well as the carbonyl compounds are reactive in the hydrotreating process from lower temperature values of 250°C. Meanwhile, the carboxylic compounds have a lower reactivity in the deoxygenation at temperature value of 250°C, thus the hydrotreating process of these compounds begins at temperatures above 300°C.

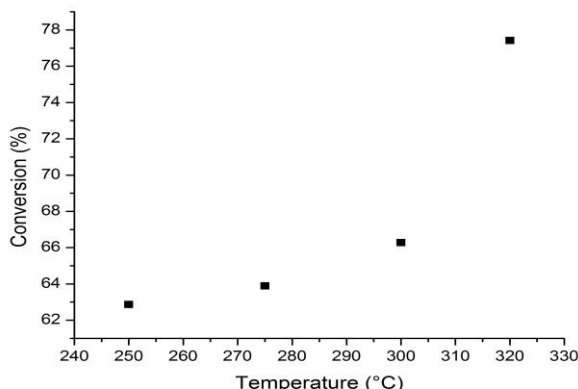


Figure 6. The influence of temperature over bio-oil conversion

Figure 7 presents the yields in products composition of liquid organic phase resulted after bio-oil hydrotreating process. The yields in the C₆-C₈ hydrocarbon and furan fractions have similar values at temperatures up to 275°C, after which the yield in furans decreases slightly with temperature reaching about 10 % at 320°C, due to their lower reactivity in the hydrodeoxygenation process. The yield of fatty acid composition decreases with increasing temperature reaching the lowest value about 5% at 320°C. The yield in the C₁₅-C₁₈ hydrocarbon fraction increases with increasing temperature, perhaps due to the hydro-decarboxylation reaction of the fatty acids from the waste vegetable oil fraction. As expected, the total acid number of hydrotreated bio-oil decreases with temperature with almost 89%, from 135.9 to almost 15 mg KOH/g.

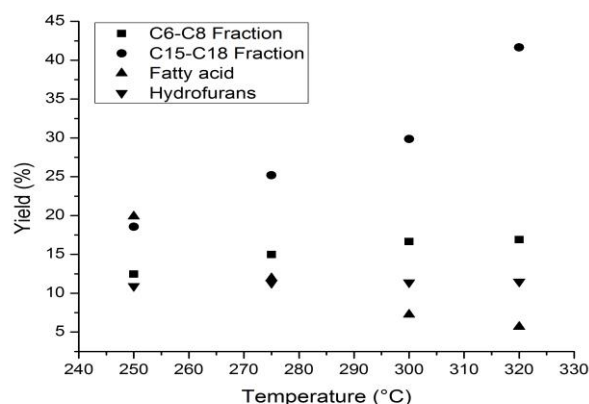


Figure 7. The influence of temperature over the yields in products composition of liquid organic phase

The second parameter studied was pressure. Figure 8 exhibits the influence of pressure in the range 20-40 bar over bio-oil conversion, at constant temperature of 320°C. The conversion of bio-oil increases with pressure, the increase being more accentuated in the range of 30-40 bar. It is observed that low pressures (20-30 bar) favors preferentially the hydrodeoxygenation reaction of carbonyl and phenolic compounds, while higher pressures hydrodeoxygenate the carboxylic compounds. Therefore, at 20 bar the bio-oil conversion was of 77.42 and increased to 87.23% at 40 bar.

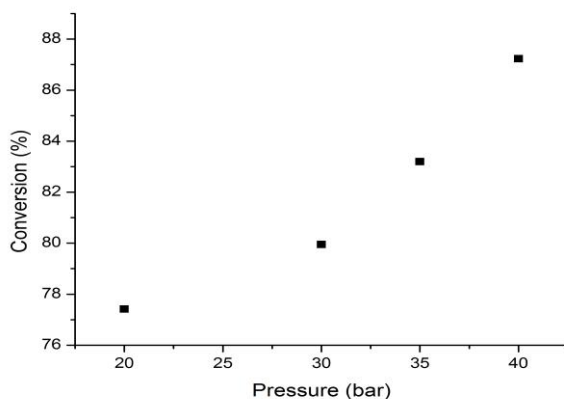


Figure 8. The influence of temperature over bio-oil conversion

Regarding the yields in products composition, high pressure favors the decarboxylation of the lipids and fatty acids, so that the yield in the C₁₅-C₁₈ hydrocarbon fraction increases from 41.64 at 20 bar to maximum value of 50.79 at 40 bar. In contrast, the yield in C₆-C₈ fraction, resulting mainly from the hydrotreating of phenols and carbonyl compounds, is not significantly influenced by the pressure variation, the growth being slightly. The yield in furans does not change practically on the studied pressure range, the efficiency of the catalyst studied in the hydrotreating process of furans being relatively low at these pressure values (Fig. 9). The total acid number of the hydrotreated bio-oil decreases with the increase of the pressure, behavior explained by the increase activity of the Co-Mo catalyst, at pressure over 30 bar, for hydro-decarboxylation process.

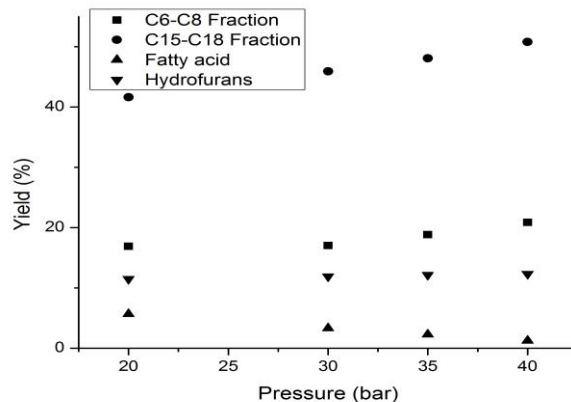


Figure 9. The influence of temperature over the yields in products composition of liquid organic phase

Evaluation of main noxious emissions of bio-oil hydrotreating gaseous phase

After each experiment, the gas-phase composition was analyzed, and the most representative data are given in table 4. The main component of gaseous phase is unreacted hydrogen, followed by CO and C₁-C₄ hydrocarbons in different percent depending on the experimental parameters used.

Unlike natural gas which has been intensively studied in the combustion process, synthesis gas fuel mixtures have not been widely investigated. Therefore, an evaluation of main noxious emissions was performed through a pure chemical modeling algorithm developed. This chemical modeling algorithm allows to chemically analyzing the constant pressure combustion for any gaseous mixture fuels. The chemical model chose the minimum and necessary chemical equations in order to quantify the air based combustion noxious.

The main combustion noxious emissions, i.e. CO, NO and NO₂, for the gaseous mixture fuel were evaluated through a combustion chemistry model involving the energy and mass balance equations applied to three type of chemical reactions:

- primary oxidation of inlet chemical species of gaseous fuel,
- secondary dissociation chemical reactions and,
- tertiary recombination chemical reactions.

The combustion was thought to be made in two successive fictitious steps complying with energy and mass balance laws, see Figure 10.

- the first step is an isothermal and constant pressure combustion at the standard temperature $T_0 = 298$ K and at an imposed pressure $p \geq p_0$, with $p_0 = 0.1$ MPa; this step is performed inside an isothermal fictitious combustion space, IFCS, and it is conceived without dissociation;
- the second step is a heating with dissociation of flue gases produced in the first step; this process takes place inside the second fictitious heating and dissociation space, FHDS, and here it is consuming the heat released in the first step, i.e. the higher heating value HHV.

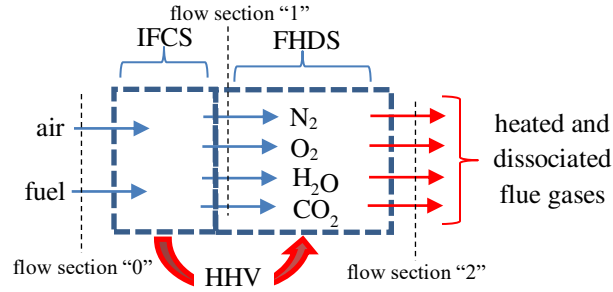
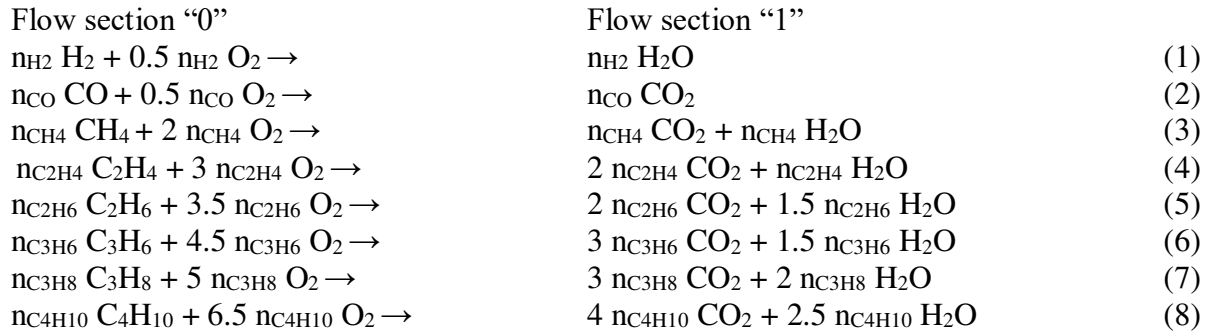


Figure 10. The scheme of the combustion process

The combustion inside IFCS

The mass balance for IFCS considers chemical oxidation reactions without dissociation of the gaseous fuel. The mass balance allowed the computation of inlet and outlet mole fractions of all chemical species. The table 4 includes the mole fractions in the flow section “0” and the Table 5 includes the mole fractions in the flow section “1”.

The primary chemical oxidation reactions inside IFCS



The above chemical reactions give the following kmole cumulative values:



where

$$n_{O_2,min} = 0.5 n_{H_2} + 0.5 n_{CO} + 2 n_{CH_4} + 3 n_{C_2H_4} + 3.5 n_{C_2H_6} + 4.5 n_{C_3H_6} + 5 n_{C_3H_8} + 6.5 n_{C_4H_{10}} \quad (9)$$

$$n_{N_2,min} = 3.7619 n_{O_2,min} \quad (10)$$

$$y_{CO_2} = n_{CO} + n_{CH_4} + 2 n_{C_2H_4} + 2 n_{C_2H_6} + 3 n_{C_3H_6} + 3 n_{C_3H_8} + 4 n_{C_4H_{10}} \quad (11)$$

$$z_{H_2O} = 0.5 n_{H_2} + n_{CH_4} + n_{C_2H_4} + 1.5 n_{C_2H_6} + 1.5 n_{C_3H_6} + 2 n_{C_3H_8} + 2.5 n_{C_4H_{10}} \quad (12)$$

Table 4. The mole composition in the flow section “0”.

Fuel $N_f = 1$ kmole								Air	
n_{H_2} [kmole]	n_{CO} [kmole]	n_{CH_4} [kmole]	$n_{C_2H_4}$ [kmole]	$n_{C_2H_6}$ [kmole]	$n_{C_3H_6}$ [kmole]	$n_{C_3H_8}$ [kmole]	$n_{C_4H_{10}}$ [kmole]	n_{O_2} [kmole]	n_{N_2} [kmole]
0.27867	0.161	0.45878	0.03589	0.01879	0.01335	0.006222	0.0273	$(1+x)n_{O_2,min}$	$(1+x)n_{N_2,min}$

where $n_{O_2,min} = 1.5795$ kmole, $n_{N_2,min} = 5.9418$ kmole and x is the excess air/oxygen

Table 5. The mole composition in the flow section ”1”.

y_{CO_2} [kmole]	z_{H_2O} [kmole]	r_{O_2} [kmole]	r_{N_2} [kmole]
0.89706	0.762916	$1.5795x$	$5.9418(1+x)$

The energy balance for IFCS computed the value of the combustion higher heating value, HHV, released by the constant temperature and constant pressure combustion of the fuel.

$$\sum_{outlet} N_i \cdot h_{f,i}^0 - \sum_{inlet} N_j \cdot h_{f,j}^0 = HHV \quad [kJ/kmole]$$

N_i and $h_{f,i}^0$ are the kmole number and the standard enthalpy of formation for each outlet chemical species, N_j and $h_{f,j}^0$ are the kmole number and the standard enthalpy of formation for each inlet chemical species. Thus it is yielding, see Table 6:

$$HHV = y_{CO_2} \cdot h_{f,CO_2}^0 + z_{H_2O} \cdot h_{f,H_2O}^0 - n_{CO} \cdot h_{f,CO}^0 - n_{CH_4} \cdot h_{f,CH_4}^0 - n_{C_2H_4} \cdot h_{f,C_2H_4}^0 - n_{C_2H_6} \cdot h_{f,C_2H_6}^0 - n_{C_3H_6} \cdot h_{f,C_3H_6}^0 - n_{C_3H_8} \cdot h_{f,C_3H_8}^0 - n_{CO} \cdot h_{f,C_4H_{10}}^0 = -5.15403 \cdot 10^5 \quad [kJ/kmole] \quad (13)$$

Table 6. The enthalpy of formation of chemical species in the flow sections “0”, “1”
 $p_0 = p_1 = 0.8$ MPa, $T_0 = T_1 = 298$ K, [25-31]

h_{f,O_2}^0 [kJ/kmole]	h_{f,N_2}^0 [kJ/kmole]	h_{f,H_2}^0 [kJ/kmole]	$h_{f,CO}^0$ [kJ/kmole]	h_{f,CO_2}^0 [kJ/kmole]	h_{f,CH_4}^0 [kJ/kmole]	$h_{f,C_2H_4}^0$ [kJ/kmole]	$h_{f,C_2H_6}^0$ [kJ/kmole]	$h_{f,C_3H_6}^0$ [kJ/kmole]	$h_{f,C_3H_8}^0$ [kJ/kmole]	$h_{f,C_4H_{10}}^0$ [kJ/kmole]	h_{f,H_2O}^0 [kJ/kmole]
0	0	0	-110527	-393522	-74873	+52467	-84740	+20430	-103900	-126800	-285830

The flue gases heating with dissociation inside FHDS

The non-dissociated flue gases leaving the IFCS enter the FHDS where take place two simultaneous processes:

- chemical reactions of dissociation and recombination controlled by chemical equilibrium constants and
- constant pressure heating of all chemical species, non or dissociated ones.

The both processes are completed by consuming the HHV. The flow scheme asked by the mass and energy balance laws is presented in the Figure 11. They were considered the below chemical reactions of dissociation and recombination.



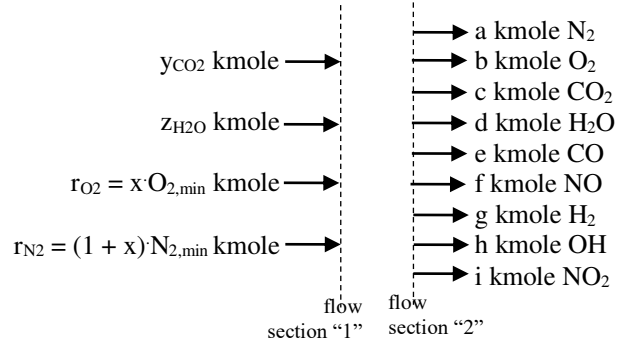


Figure 11. The inlet/outlet flow scheme of chemical species for FHDS

The mass balance for FHDS gives the following four dependences:

$$a = r_{N_2} - 0.5f - 0.5i \quad (19)$$

$$b = r_{O_2} - 0.5f - i + 0.5e + 0.5g \quad (21)$$

$$c = y_{CO_2} - e \quad (22)$$

$$d = z_{H_2O} - g - h \quad (23)$$

The mass balance is completed through chemical equilibrium constants K .

$$v_A \cdot A + v_B \cdot B \rightarrow v_C \cdot C + v_D \cdot D \Rightarrow K = \frac{C^{v_C} \cdot D^{v_D}}{A^{v_A} \cdot B^{v_B}} \cdot \left(\frac{p}{p_0} \right)^{v_C + v_D - v_A - v_B}$$

Therefore they are yielding:

– dissociation of CO_2

$$K1 = \frac{e^2 \cdot b}{c^2} \cdot \left(\frac{p}{p_0} \right)^{2+1-2} = \frac{e^2 \cdot b}{c^2} \cdot \left(\frac{p}{p_0} \right) \Rightarrow e = \left(\frac{K1 \cdot c^2 \cdot p_0}{b \cdot p} \right)^{0.5} \quad (24)$$

– dissociation of H_2O giving OH and H_2

$$K2 = \frac{g^2 \cdot b}{d^2} \cdot \left(\frac{p}{p_0} \right)^{2+1-2} = \frac{g^2 \cdot b}{d^2} \cdot \left(\frac{p}{p_0} \right) \Rightarrow g = \left(\frac{K2 \cdot d^2 \cdot p_0}{b \cdot p} \right)^{0.5} \quad (25)$$

– dissociation of H_2O giving H_2 and O_2

$$K3 = \frac{h^2 \cdot g}{d^2} \cdot \left(\frac{p}{p_0} \right)^{2+1-2} = \frac{h^2 \cdot g}{d^2} \cdot \left(\frac{p}{p_0} \right) \Rightarrow h = \left(\frac{K3 \cdot d^2 \cdot p_0}{g \cdot p} \right)^{0.5} \quad (26)$$

– recombination of N_2 and O_2 giving NO

$$K4 = \frac{f^2}{a \cdot b} \cdot \left(\frac{p}{p_0} \right)^{2-1-1} = \frac{f^2}{a \cdot b} \Rightarrow f = (K4 \cdot a \cdot b)^{0.5} \quad (27)$$

– recombination of N_2 and O_2 giving NO_2

$$K5 = \frac{i^2}{a \cdot b^2} \cdot \left(\frac{p}{p_0} \right)^{2-1-2} = \frac{i^2}{a \cdot b^2} \cdot \left(\frac{p_0}{p} \right) \Rightarrow i = \left(\frac{K5 \cdot a \cdot b^2 \cdot p}{p_0} \right)^{0.5} \quad (28)$$

The equations 19 to 28 could be solved if they are known the flue gases temperature, T_{fg} , in the flow section “2” and the excess air, x , in the flow section “1”.

The energy balance gives the extra dependence between unknown mole composition of flue gases leaving FHDS and T_{fg} and x .

$$\begin{aligned}
 & a \cdot \int_{T_0}^{T_{fg}} c_{p,N_2} \cdot dT + b \cdot \int_{T_0}^{T_{fg}} c_{p,O_2} \cdot dT + c \cdot \left(h_{f,CO_2}^0 + \int_{T_0}^{T_{fg}} c_{p,CO_2} \cdot dT \right) + d \cdot \left(h_{f,H_2O}^0 + \int_{T_0}^{T_{fg}} c_{p,H_2O} \cdot dT \right) \\
 & + e \cdot \left(h_{f,CO}^0 + \int_{T_0}^{T_{fg}} c_{p,CO} \cdot dT \right) + f \cdot \left(h_{f,NO}^0 + \int_{T_0}^{T_{fg}} c_{p,NO} \cdot dT \right) + (g + 0.5 \cdot h) \cdot \int_{T_0}^{T_{fg}} c_{p,H_2} \cdot dT \\
 & + h \cdot \left(h_{f,OH}^0 + \int_{T_0}^{T_{fg}} c_{p,OH} \cdot dT \right) + i \cdot \left(h_{f,NO_2}^0 + \int_{T_0}^{T_{fg}} c_{p,NO_2} \cdot dT \right) - y_{CO_2} \cdot h_{f,CO_2}^0 - z_{H_2O} \cdot h_{f,H_2O}^0 = |HHV|
 \end{aligned} \tag{29}$$

The specific heat capacities, c_p , were approximated by polynomial dependences on temperature.

The enthalpies of formation of new chemical species are included in the Table 7.

Table 7. The enthalpy of formation of chemical species in the flow sections “2”
 $p_0 = p_1 = p_2 = 0.8 \text{ MPa}$, $T_0 = T_1 = 298 \text{ K}$, $T_2 = T_{fg}$, [25-31]

h_{f,O_2}^0	h_{f,N_2}^0	h_{f,H_2}^0	$h_{f,CO}^0$	h_{f,CO_2}^0	$h_{f,NO}^0$	h_{f,NO_2}^0	$h_{f,OH}^0$	h_{f,H_2O}^0
[kJ/kmole]	[kJ/kmole]	[kJ/kmole]	[kJ/kmole]	[kJ/kmole]	[kJ/kmole]	[kJ/kmole]	[kJ/kmole]	[kJ/kmole]
0	0	0	-110527	-393522	+90291	+33100	+38897	-285830

Because the equations 19 to 28 includes large quantities, i.e. a , b , c , d , and small, very small or negligible quantities, i.e. e , f , g , h , i , the computational procedure starts with equations 24 to 28 in which they were imposed the temperature T_{fg} and supposed that $a \approx r_{N_2}$, $b \approx r_{O_2}$, $c \approx y_{CO_2}$ and $d \approx z_{H_2O}$. The preliminary evaluation of e , f , g , h and i allows the first evaluation of a , b , c and d through equations 19 to 23 followed by a preliminary evaluation of excess air through equation 29. Knowing the first values of all chemical species and x , the next step re-uses the equations 24 to 28 and after those equations 19 to 23 and 29. The iterative procedure is finished when the imposed error between two successive iterations is reached. The numerical results are included in the Table 8.1. and 8.2.

Table 8.1. The mole composition of flue gases function of temperature T_{fg} , flow section “2”
 $p_2 = 0.8 \text{ MPa}$

x	T_{fg}	e_{CO}	f_{NO}	g_{H_2}	h_{OH}	i_{NO_2}
[kmole/kmole fuel]	[K]	[kmole/kmole fuel]	[kmole/kmole fuel]	[kmole/kmole fuel]	[kmole/kmole fuel]	[kmole/kmole fuel]
10.425	500	$7.417 \cdot 10^{-27}$	$5.505 \cdot 10^{-8}$	$1.937 \cdot 10^{-25}$	$4.548 \cdot 10^{-15}$	$1.0211 \cdot 10^{-5}$
2.0625	1000	$1.0657 \cdot 10^{-11}$	$6.665 \cdot 10^{-4}$	$1.3063 \cdot 10^{-11}$	$3.907 \cdot 10^{-7}$	$4.88 \cdot 10^{-5}$
1.3175	1200	$3.822 \cdot 10^{-9}$	$2.841 \cdot 10^{-3}$	$2.376 \cdot 10^{-9}$	$9.031 \cdot 10^{-6}$	$5.16 \cdot 10^{-5}$
0.855	1400	$2.668 \cdot 10^{-7}$	$7.469 \cdot 10^{-3}$	$1.049 \cdot 10^{-7}$	$8.295 \cdot 10^{-5}$	$4.7472 \cdot 10^{-5}$
0.547	1600	$6.796 \cdot 10^{-6}$	$1.4379 \cdot 10^{-2}$	$1.9308 \cdot 10^{-6}$	$4.243 \cdot 10^{-4}$	$3.914 \cdot 10^{-5}$
0.3345	1800	$9.024 \cdot 10^{-5}$	$2.211 \cdot 10^{-2}$	$2.0188 \cdot 10^{-5}$	$1.453 \cdot 10^{-3}$	$2.891 \cdot 10^{-5}$
0.1835	2000	$1.226 \cdot 10^{-4}$	$1.531 \cdot 10^{-2}$	$2.746 \cdot 10^{-5}$	$1.245 \cdot 10^{-3}$	$1.471 \cdot 10^{-5}$
0.0765	2200	$5.607 \cdot 10^{-3}$	$2.756 \cdot 10^{-2}$	$1.07 \cdot 10^{-3}$	$7.654 \cdot 10^{-3}$	$8.304 \cdot 10^{-6}$

Table 8.2. The mole composition of flue gases function of temperature T_{fg} , flow section “2”
 $p_2 = 0.1$ MPa

x [kmole/kmole fuel]	T_{fg} [K]	e_{CO} [kmole/kmole fuel]	f_{NO} [kmole/kmole fuel]	g_{H_2} [kmole/kmole fuel]	h_{OH} [kmole/kmole fuel]	i_{NO_2} [kmole/kmole fuel]
10.425	500	$2.098 \cdot 10^{-26}$	$5.505 \cdot 10^{-8}$	$5.479 \cdot 10^{-25}$	$7.649 \cdot 10^{-15}$	$2.888 \cdot 10^{-5}$
2.0625	1000	$3.014 \cdot 10^{-11}$	$6.665 \cdot 10^{-4}$	$3.694 \cdot 10^{-11}$	$6.571 \cdot 10^{-7}$	$1.38 \cdot 10^{-4}$
1.3175	1200	$1.081 \cdot 10^{-8}$	$2.840 \cdot 10^{-3}$	$6.720 \cdot 10^{-9}$	$1.518 \cdot 10^{-5}$	$1.459 \cdot 10^{-4}$
0.855	1400	$7.547 \cdot 10^{-7}$	$7.47 \cdot 10^{-3}$	$2.967 \cdot 10^{-7}$	$1.395 \cdot 10^{-4}$	$1.343 \cdot 10^{-4}$
0.5472	1600	$1.922 \cdot 10^{-5}$	$1.438 \cdot 10^{-2}$	$5.461 \cdot 10^{-6}$	$7.136 \cdot 10^{-4}$	$1.107 \cdot 10^{-4}$
0.3335	1800	$2.557 \cdot 10^{-4}$	$2.205 \cdot 10^{-2}$	$5.704 \cdot 10^{-5}$	$2.437 \cdot 10^{-3}$	$8.136 \cdot 10^{-5}$
0.1825	2000	$3.461 \cdot 10^{-4}$	$1.532 \cdot 10^{-2}$	$7.756 \cdot 10^{-5}$	$2.095 \cdot 10^{-3}$	$4.168 \cdot 10^{-5}$
0.0670	2200	$1.652 \cdot 10^{-2}$	$2.636 \cdot 10^{-2}$	$2.679 \cdot 10^{-3}$	$1.162 \cdot 10^{-2}$	$2.157 \cdot 10^{-5}$

Tables 8.1 and 8.2 present the main combustion noxious emissions, i.e. CO, NO and NO₂ calculated using the chemical modeling algorithm at different temperatures, pressure and excess of air/oxygen. The emission levels calculated using the model had in most cases the same variation trend. For example, at high excess of air/oxygen and low temperature the emission of CO, NO and NO₂ calculated have the minimum values. This result was expected, as the combustion process was performed under conditions of high oxygen excess that maximize the formation of complete combustion products. Opposite, at low air/oxygen excess and high temperature, the combustion noxious emission presents maximum values, but in most cases, above the legal limit. However, emissions under hydrotreating conditions should not be compared with proposals within legal limits, since these limits refer mainly to combustion conditions with excess air [32]. The gaseous fraction resulted from hydrotreating experiments contains a high amount of unreacted hydrogen. In conclusion, the model developed allows the evaluation of harmful emissions depending on the temperature and pressure set on the flue gases. This calculation algorithm can be applied to any pressurized or atmospheric combustion engine fueled with different mixture of combustible gases such as: natural gas, hydrogen-enriched natural gas or oxy-fuel.

Methods

Catalyst preparation

The HMS material was synthesized via templating pathway using tetraethylorthosilicate (TEOS) as silica source and dodecylamine (DDA, Merck) as template and ethanol (EtOH) and water as solvents. Tetraethylorthosilicate (TEOS) was added to a mixture of dodecylamine (DDA), water and ethanol at room temperature. The mixture was stirred for 1 h at 40°C and then let for 24h at 25°C. The molar composition of the material was 1.0 SiO₂: 0.27 DDA: 8.5 EtOH: 29 H₂O. The solid was filtered, washed, dried at room temperature and calcined in air at 550°C for 8h (1°C/min), to remove the template. The γ -Al₂O₃-HMS support was obtained as cylindrical extrudates with the average size of 2 mm. The powdered materials (γ -Al₂O₃/HMS: 40/60) were mixed with a 10% (wt%) HNO₃ solution, which is gradually dosed, for 1 hour. After dosing the nitric acid, stirring is continued for 3 hours at ambient temperature. The resulted homogeneous paste is inserted into a manually operated extruder with interchangeable diameters, the diameter of a die having the size of 1 mm. The resulted extrudates were dried for 6 h at 160 °C and annealed at 450 °C (10°C/min). The molybdenum (8%) and cobalt (4%) catalyst was prepared by incipient wetness impregnation method using appropriate concentrations of aqueous solutions

of ammonium heptamolybdate ((NH₄)₆Mo₇O₂₄, Aldrich 99%) and cobalt (II) nitrate hexahydrate (Co(NO₃)₂·6H₂O), Aldrich 98%). After impregnation on γ -Al₂O₃-HMS support the wet cylinders were dried at 120°C for 4 h and calcined at 450°C for 2 h.

Catalyst characterization

Textural properties of the catalysts were analyzed by using Nitrogen sorption measurements carried out at 77 K in a Nova 1000 Quantachrome instrument. Prior to analysis, the samples were heated to 200 °C for 1 h. The X-ray diffraction (XRD) analysis was carried out using a fully automated, modular Rigaku Smart Labdiffractometer, operated at 45 kV and 200 mA, with Cu K α radiation (1.54059 Å), parallel beam configuration (2 θ / θ scan mode) and scanning range between 2–90° (2 θ), with a 0.02° step. Fourier transform infrared (FT-IR) analysis was performed with a FT-IR Tensor 27 - Bruker spectrometer, using KBr pellet technique [32]. Microscopy (SEM) analysis was conducted using a FEI Inspect, S model microscope and FTIR using Jasco 610 spectrometer, with a scanning range from 4000 to 400 cm⁻¹, a scan rate of 4 cm⁻¹·s⁻¹ and an average of 64 measurements in the final spectrum. The X-Ray Photoelectron Spectroscopy (XPS) spectra were obtained on a SPECS spectrometer by using the Al anode (1486.6 eV) radiation.

Catalytic tests

The activity tests of 4%Co8%Mo/ γ -Al₂O₃-HMS catalyst were carried out in a fixed bed flow reactor (length of 0.5 m, volume of 200 cm³) heated by an electrical furnace. An amount of 50 cm³ catalyst was loaded in the middle zone of the reactor. The catalyst was activated in situ with a flow rate of 15 L/h hydrogen at 450 °C for 6 h. The bio-oil used in this report was obtained by pyrolysis of biomass derivate from biogas process and conditioned with waste vegetable oil. Bio-oil was introduced into the reactor using a metering pump, mixed with H₂, and preheated to a desired temperature. The liquid samples were analyzed by GC/MS 7000 Triple Quad MS (Agilent Technologies) system equipped with HP-FFAP (30m, 250 μ m, 0.25 μ m) column and He as carrier gas with volumetric flow of 1 ml/min. The oven program started from 30 °C with 2°C/min rate and until reached 100°C. The injector temperature was set at 250 °C. The compounds were identified using NIST MS Search 2.0 Library. The water content in the samples was determined by Karl Fischer method (ASTM D6869). Density, total acid number and saponification number were determined using standardized methods [33].

The gaseous fraction generated during the experiments was analyzed using a Agilent Technologies 6890N Gas-Chromatograph with a Thermal Conductivity Detector (TCD), connected on-line, equipped with a SHINCARBON ST 80/100 2M, 2M ID,1/8"OD, SILCO, HP column and He as carrier gas with volumetric flow of 50mL/min. The column temperature was set up to 40°C (hold time) 300°C, program rate: 20°C/min, injection temperature: 300°C, detector temperature 300°C, sample volume: 0.75 mL.

The product yields in were calculated using the following equations:

$$\eta_i(\%) = \frac{\frac{x_i \cdot \bar{M}_{oil}}{M_i}}{\left(\sum_{i=1}^n \frac{x_i \cdot \bar{M}_{oil}}{M_i}\right) + x_{unreacted}} \cdot 100$$

Where,

\bar{M}_{oil} -average molecular weight of the bio-oil

X_i -mass fraction of the component i
 M_i -molecular weight of component i

$$\text{Conversion}(\%) = \sum_i^n \eta_i(\%)$$

References

1. Wiśniewski, D., Gołaszewski, J., Białowiec, A. The pyrolysis and gasification of digestate from agricultural biogas plant. *Archives of Environmental Protection*. **41**, 70–75 (2015).
2. Hosseini Koupaie, E., Azizi, A., Bazyar Lakeh, A.A., Hafez, H., Elbeshbishy, E. Comparison of liquid and dewatered digestate as inoculum for anaerobic digestion of organic solid wastes. *Waste Manag.* **87**, 228-236 (2019).
3. Jung-Hun, K., Jeong-Ik, O., Yiu Fai, T., Young-Kwon, P., Jechan, L., Eilhann, E. K. CO₂-assisted catalytic pyrolysis of digestate with steel slag. *Energy*. **191**, 116529 (2020).
4. Horáčěk, J., Kubic̃ka, D. Bio-oil hydrotreating over conventional CoMo&NiMo catalysts: The role of reaction conditions and additives. *Fuel*. **198**, 49–57 (2017).
5. Vituruch, G., Boonyawan, Y., Tanakorn, R., Sabaithip, T. Hydrotreating of Free Fatty Acid and Bio-Oil Model Compounds: Effect of Catalyst Support. *Energy Procedia*. **79**, 486 – 491 (2015).
6. Botella, L., Stankovikj, F., Sánchez, J.L., Gonzalo, A., Arauzo, J., Garcia-Pérez, M. (2018) Bio-Oil Hydrotreatment for Enhancing Solubility in Biodiesel and the Oxydation Stability of Resulting Blends. *Front. Chem.* **6**, 83 1-13, (2018)
7. Wang, H., Meyer, P.A., Santosa, D.M., Zhu, C., Olarte, M.V., Jones, S.B., Zacher, A.H. Performance and techno-economic evaluations of co-processing residual heavy fraction in bio-oil hydrotreating. *Catal. Today*. 2020, in press.
8. French, R.J., Hrdlicka, J., Baldwin, R. Mild Hydrotreating of Biomass Pyrolysis Oils to Produce a Suitable Refinery Feedstock. *Environ. Prog. Sustain.* **29**, 142-150, (2010).
9. Wildschut, J., Melián-Cabrera, I., Heeres, H.J. Catalyst studies on the hydrotreatment of fast pyrolysis oil. *Appl. Catal. B-Environ.* **99**, 298–306, (2010).
10. Cai, Q., Yu, T., Meng, X., Zhang, S. Selective generation of aromatic hydrocarbons from hydrotreating-cracking of bio-oil light fraction with MO_x modified HZSM-5 (M = Ga, Mo and Zn). *Fuel Process.* **204**, 106424, (2020).
11. Wildschut, J., Mahfud, F.H., Venderbosch, R.H., Heeres, H.J. Hydrotreatment of Fast Pyrolysis Oil Using Heterogeneous Noble-Metal Catalysts. *Ind. Eng. Chem. Res.* **48** 10324–10334, (2009).
12. Mendes, F.L., Teixeira da Silva, V., Pacheco, M.E., Toniolo, F.S., Henriques, C.A. Bio-oil hydrotreating using nickel phosphides supported on carbon-covered alumina. *Fuel*. **241**, 686–694, (2019).
13. Koike, N., Hosokai, S., Takagaki, A., Nishimura, S., Kikuchi, R., Ebitani, K. Upgrading of pyrolysis bio-oil using nickel phosphide catalysts. *J. Catal.* **333**, 115–126, (2016).
14. Guo, C., Tirumala, K., Rao, V., Reyhanitash, E., Yuan, Z., Na, C. Novel Inexpensive Transition Metal Phosphide Catalysts for Upgrading of Pyrolysis Oil via Hydrodeoxygenation. *AIChE J.* **62** (10), 3664-3672 (2016).

15. Zhong-Yu, J., Zhang, T.-Q., Shang, J.-W., Zhai, M.-Lu, Yang, H., Qiao, C.-Z., Ma X.-Q. Influence of Cu and Mo components of γ -Al₂O₃ supported nickel catalysts on hydrodeoxygenation of fatty acidmethyl esters to fuel-like hydrocarbons. *J. Fuel Chem. Technol.* **46(4)**, 427-440, 2018.
16. Ardiyanti, A. R., Khromova, S.A., Venderbosch, R.H., Yakovlev, V.A., Melián-Cabrera, I.V., Heeres, H.J. Catalytic hydrotreatment of fastpyrolysis oil using bimetallic Ni Ni-Cu catalysts on varioussupports. *Appl. Catal A: Gen.* **449**, 121–130 (2012).
17. Michio, A., Haruo, T., Kiyoshi, O., Kunio, S., Tadasuke, H., Naoyuki, T. Thermally stable nickel nickel-molybdenum alloy catalysts supported on magnesium aluminate for high temperature methanation. *Sekiyu Gakkaishi* **24(6)**, 363–370 (2008).
18. Palcheva, R., Kaluza, L., Dimitrov, L., Tyuliev, G., Avdeev, G., Jiratova, K., Spojakina, A., NiMo catalysts supported on the Nb modified mesoporous SBA-15 and HMS: Effect of thioglycolic acid addition on HDS, *Appl. Catal. A: Gen.* **520**, 24-34 (2016).
19. NIST Standard Reference Database 20, Version 4.1. <https://srdata.nist.gov/xps/>.
20. Zepeda, T.A, Pawelec, B., Obeso-Estrella, R., Díaz de León, J.N, Fuentes S, Alonso-Núñez, G., et al. Competitive HDS and HDN reactions over NiMoS/HMS-Al catalysts: Diminishing of the inhibition of HDS reaction by support modification with P. *Appl. Catal. B: Environ.* **180**, 569-579 (2016).
21. Ganta, D., Sinha, S., Haasch, R.T. 2-D Material Molybdenum Disulfide Analyzed by XPS. *Surf. Sci. Spectra* **21**, 19-27 (2014).
22. Yang, J., Liu, H., Martens, W.N., Frost, R.L. Synthesis and Characterization of Cobalt Hydroxide, Cobalt Oxyhydroxide, and Cobalt Oxide Nanodiscs. *J. Phys. Chem. C.* **114**, 111-119 (2010).
23. Turner, N.H., Single, A.M. Determination of peak positions and areas from wide-scan XPS spectra. *Surf. Interface Anal.* **15**, 215-222 (1990).
24. Zafeiratos S, Dintzer T, Teschner D, Blume R, Hävecker M, Knop-Gericke A, et al. Methanol oxidation over model cobalt catalysts: Influence of the cobalt oxidation state on the reactivity. *J. of Catal.* **269**, 309-317 (2010).
25. Borgnakke, C., Sonntag, R.E., *Fundamentals of Thermodynamics*, 8th Edition, John Wiley & Sons, 2013.
26. Ruscic, B., Pinzon, R. E., Morton, M. L., von Laszewski, G., Bittner, S., Nijssure, S. G., Amin, K.A., Minkoff, M., Wagner, A. F., Introduction to Active Thermochemical Tables: Several "Key" Enthalpies of Formation Revisited. *J. Phys. Chem. A* **108**, 9979-9997 (2004).
27. Ruscic, B., Pinzon, R. E., von Laszewski, G., Kodeboyina, D., Burcat, A., Leahy, D., Montoya, D., Wagner, A. F., Active Thermochemical Tables: Thermochemistry for the 21st Century. *J. Phys. Conf. Ser.* **16**, 561-570 (2005).
28. Ruscic, B. Active Thermochemical Tables (ATcT) values based on ver. 1.118 of the Thermochemical Network (2015); available at ATcT.anl.gov
29. Ruscic, B. Active Thermochemical Tables: Dissociation Energies of Several Homonuclear First-Row Diatomics and Related Thermochemical Values. *Theor. Chem. Acc.* **133**, 1415/1-12 (2005)
30. Klippenstein, S. J., Harding, L. B., B. Ruscic, Ab initio Computations and Active Thermochemical Tables Hand in Hand: Heats of Formation of Core Combustion Species. *J. Phys. Chem. A* **121**, 35, 6580–6602 (2017).
31. Horbaniuc, B., Marin, O., Dumitrascu, G., Charon, O., Oxygen enriched combustion in supercritical steam boilers, *Energy* **29**, 427-448 (2004).

32. Conesa, J.A., Ortuño, N. & Palmer, D. Estimation of Industrial Emissions during Pyrolysis and Combustion of Different Wastes Using Laboratory Data. *Sci Rep* **10**, 6750 (2020)
33. Enascuta, C-E., Stepan, E., Bolocan, I., Bombos, D. Calin, C., Oprescu, E.-E., Lavric, V., Simultaneous production of oil enriched in ω -3 polyunsaturated fatty acids and biodiesel from fish wastes, *J. Waste Manag.*, **75**, 205-214 (2018).
- 34., Iisa, K., French, R.J., Orton, K.A., Dutta, A., Schaidle, J.A., Production of low-oxygen bio-oil via ex situ catalytic fast pyrolysis and hydrotreating. *Fuel* **207**, 413–422 (2017).

Acknowledgement

The authors gratefully acknowledge the financial support of the UEFISCDI, Romania, in the framework of PN-III-P1-1.2-PCCDI-2017, financing contract no. 32 PCCDI/2018.

Figures

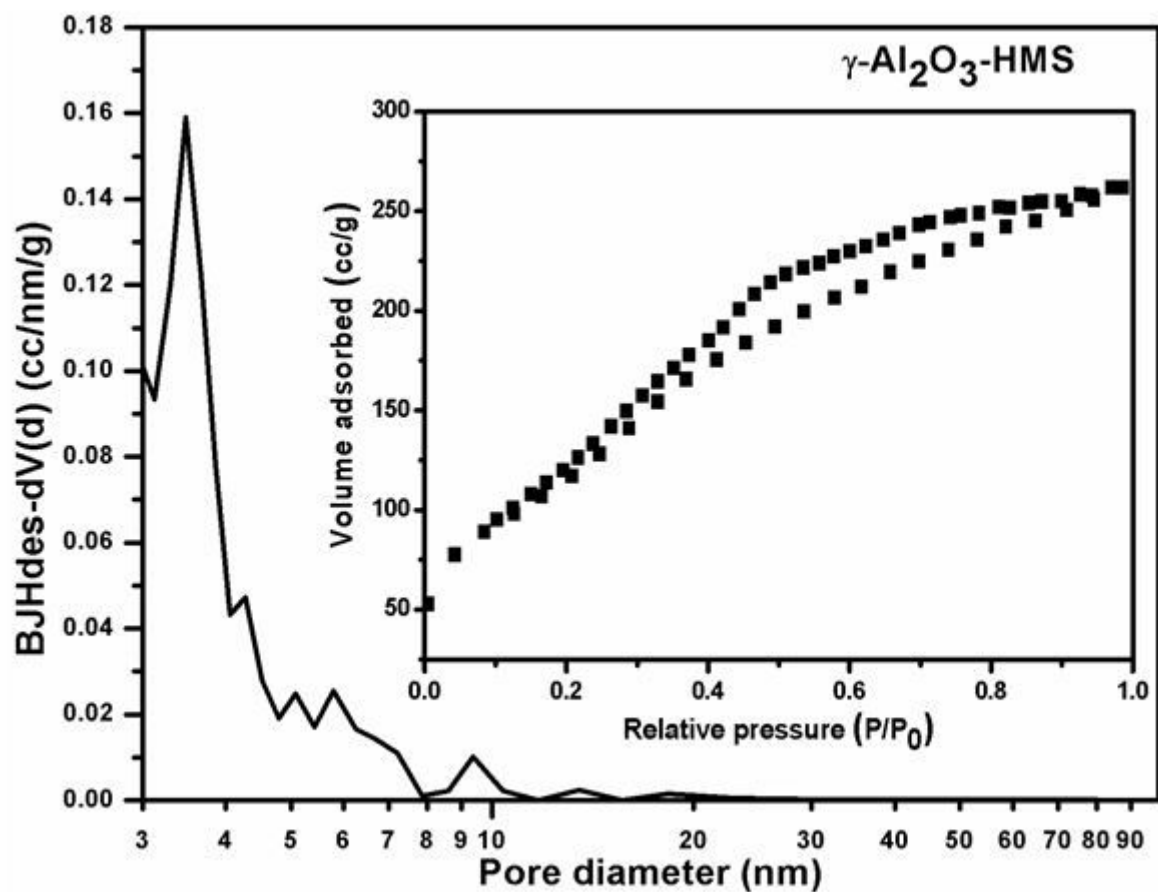


Figure 1

Please see the Manuscript PDF file for the complete figure caption.

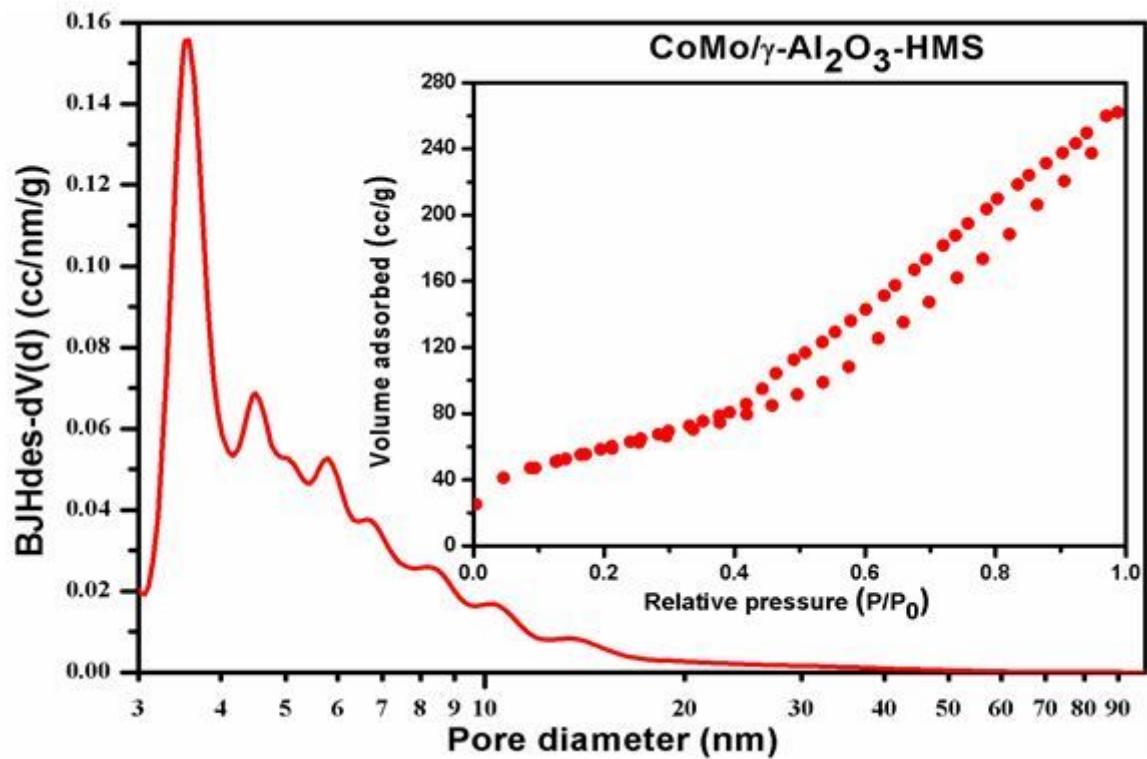


Figure 2

Please see the Manuscript PDF file for the complete figure caption.

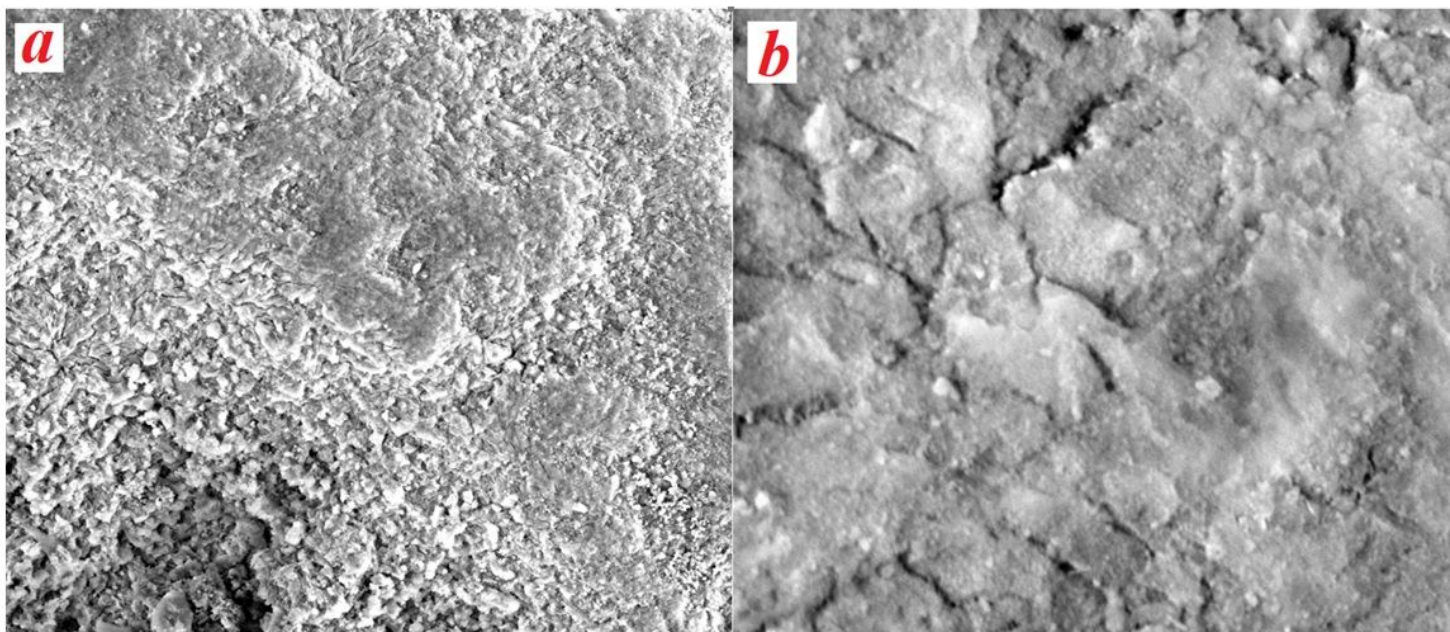


Figure 3

Please see the Manuscript PDF file for the complete figure caption.

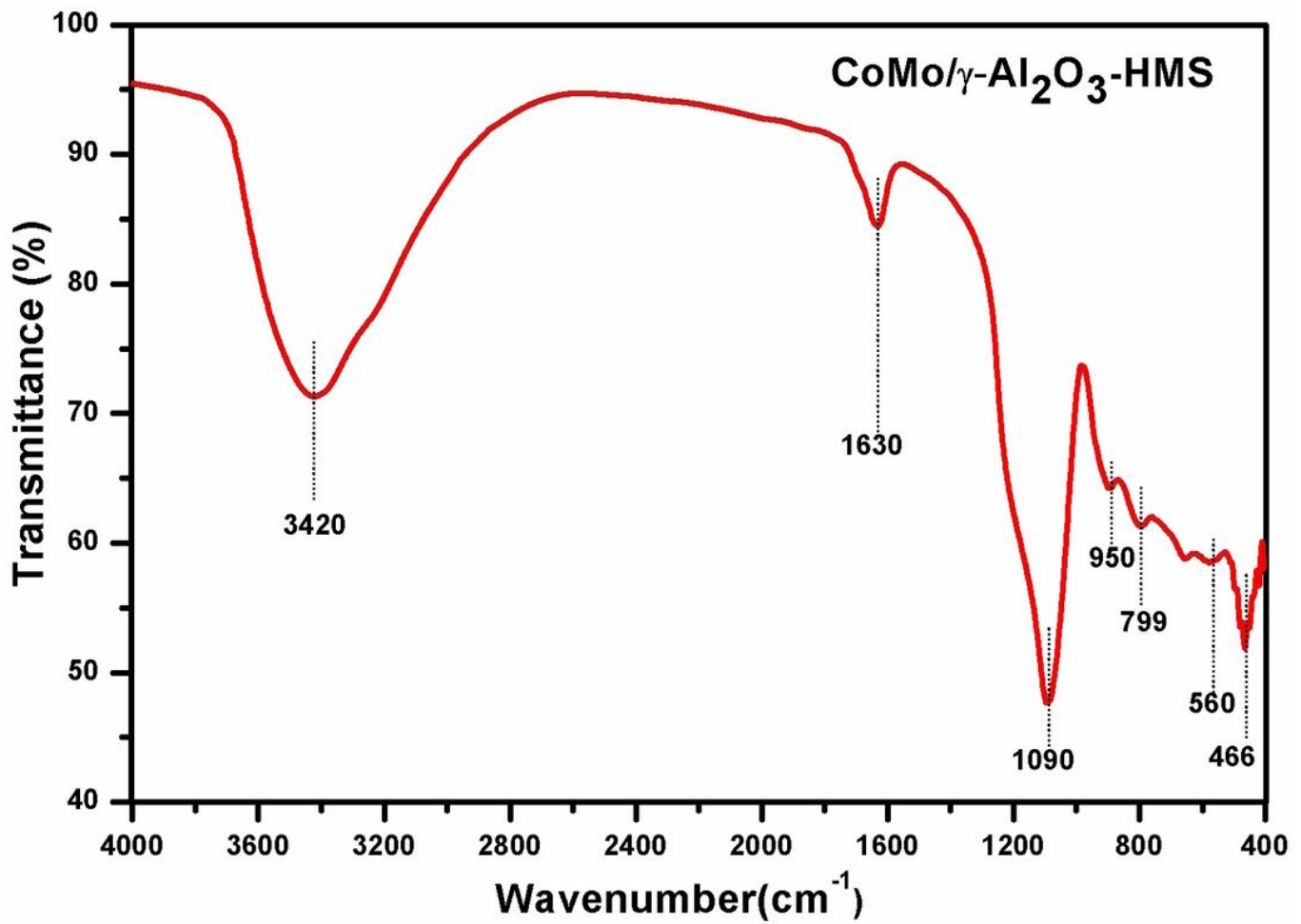


Figure 4

Please see the Manuscript PDF file for the complete figure caption.

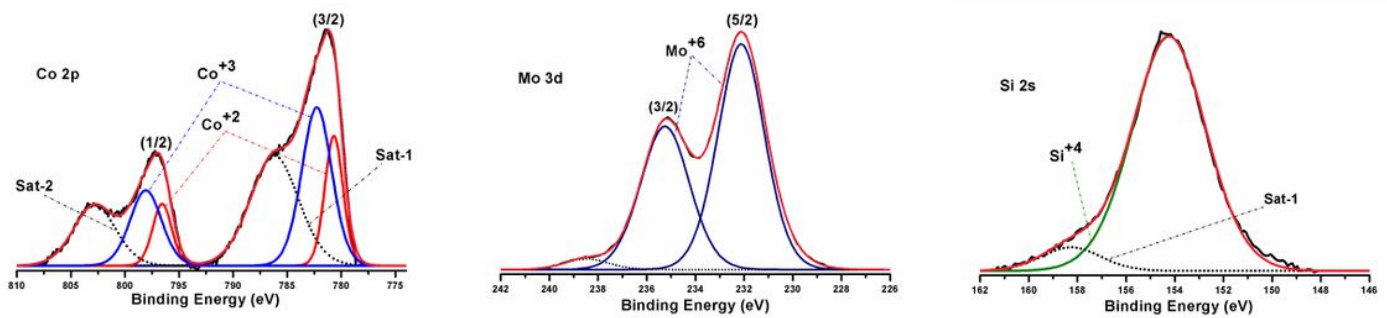


Figure 5

Please see the Manuscript PDF file for the complete figure caption.

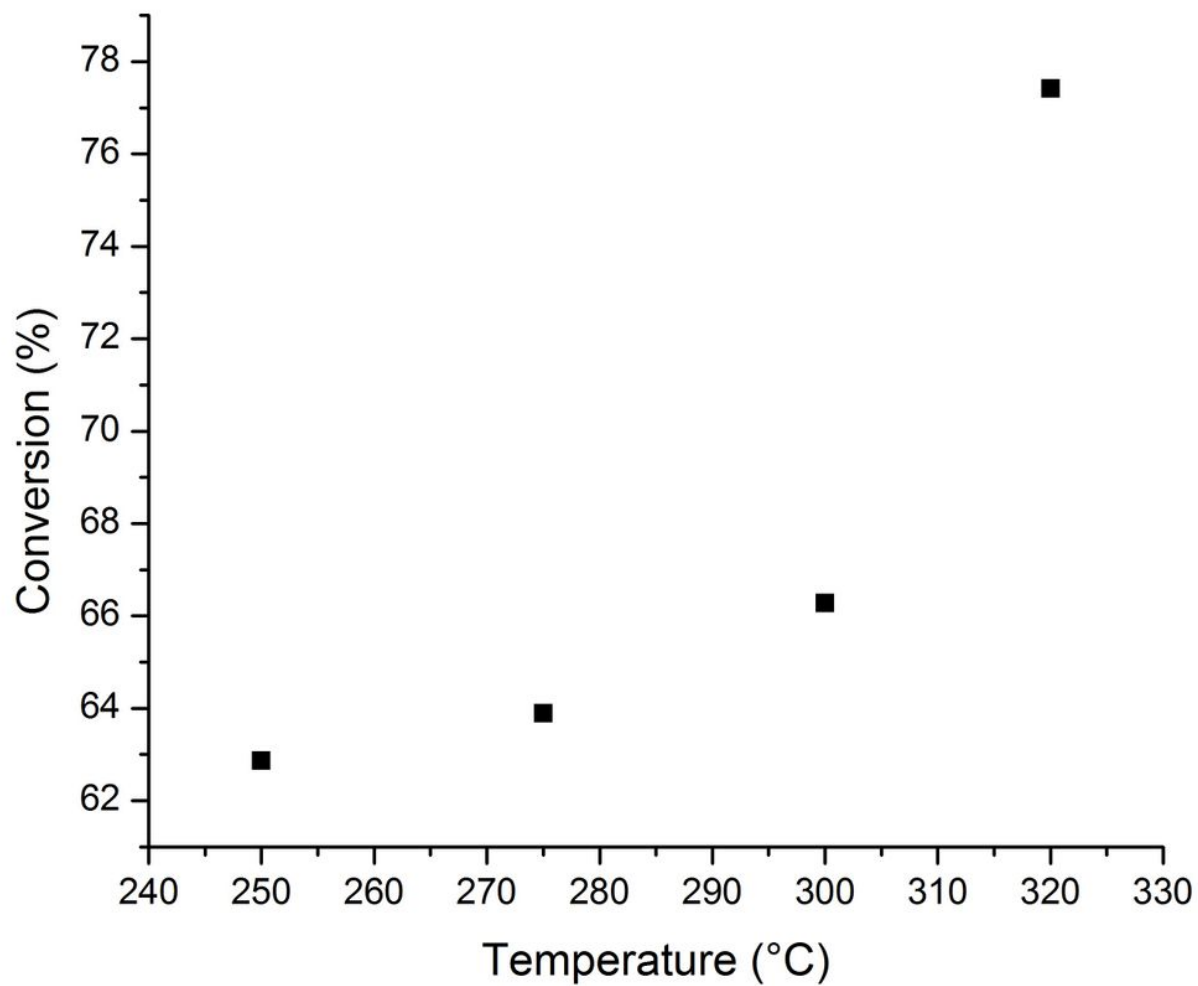


Figure 6

Please see the Manuscript PDF file for the complete figure caption.

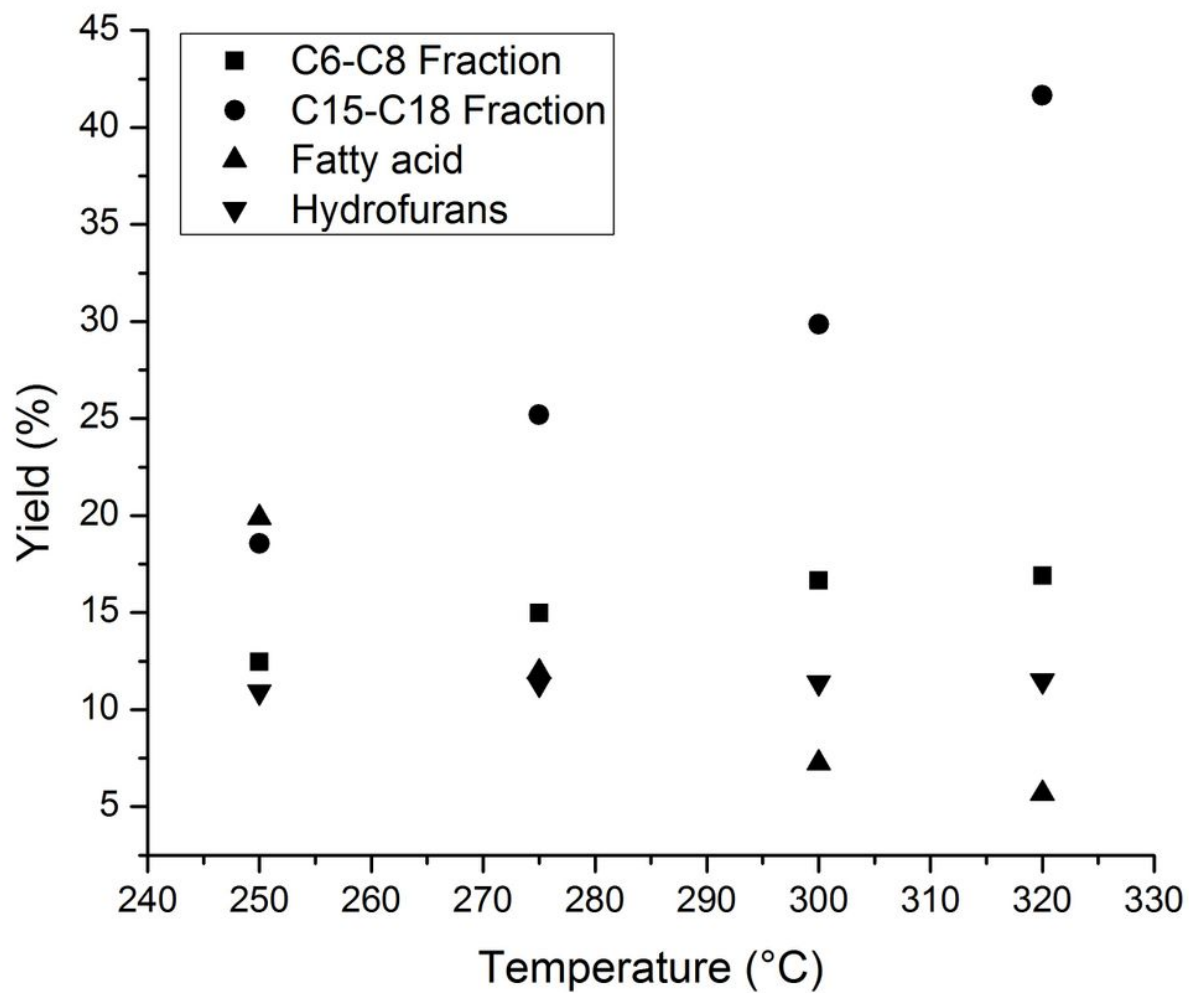


Figure 7

Please see the Manuscript PDF file for the complete figure caption.

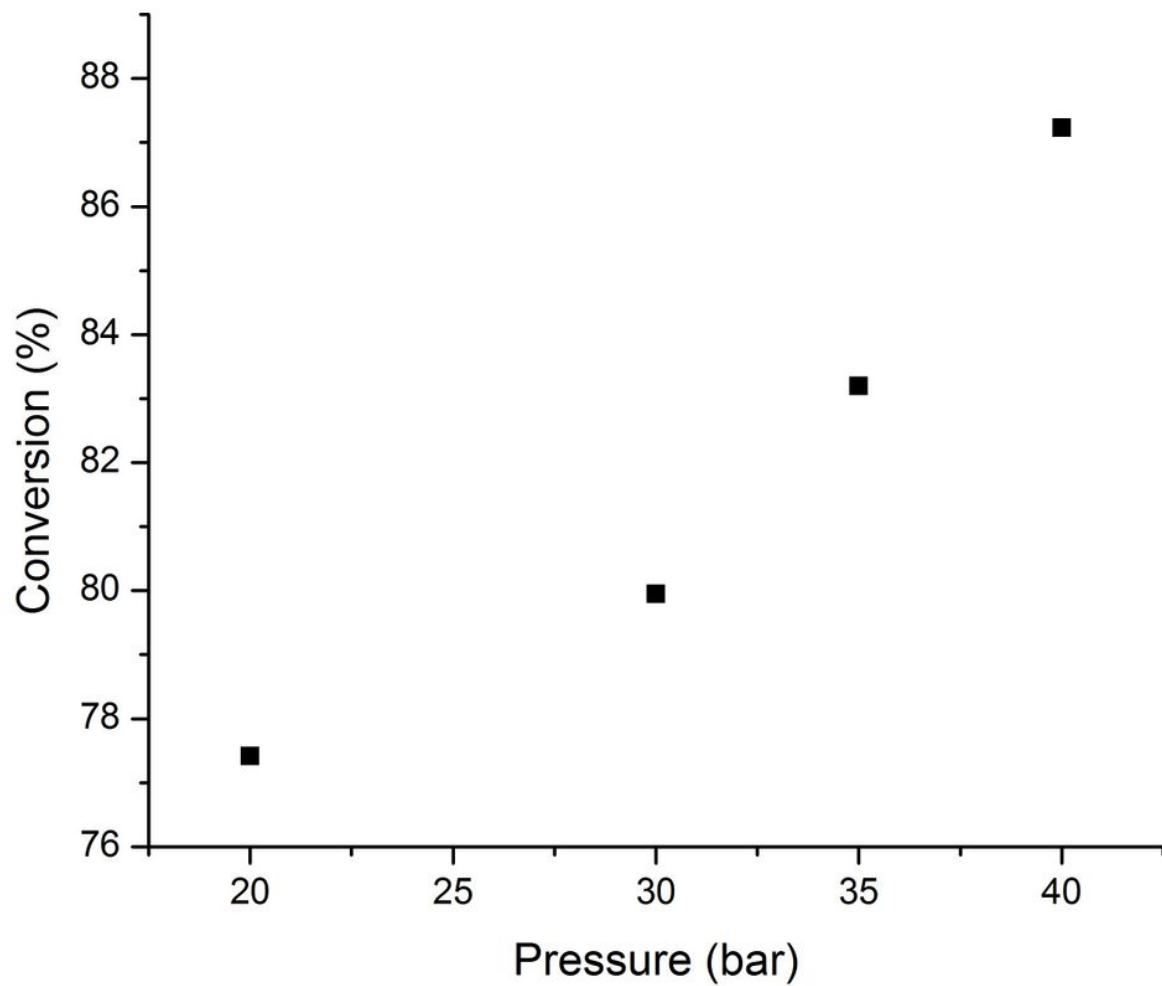


Figure 8

Please see the Manuscript PDF file for the complete figure caption.

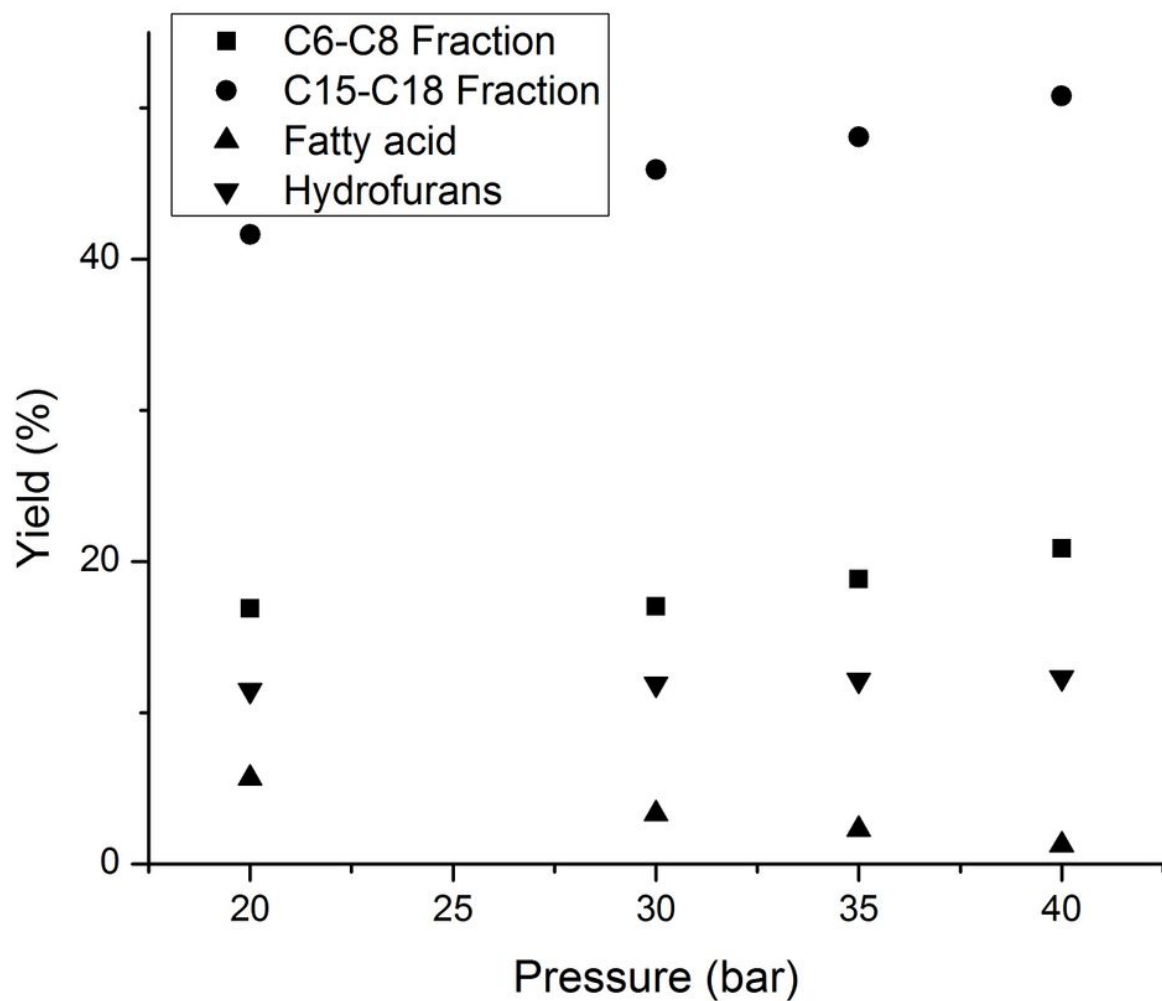


Figure 9

Please see the Manuscript PDF file for the complete figure caption.

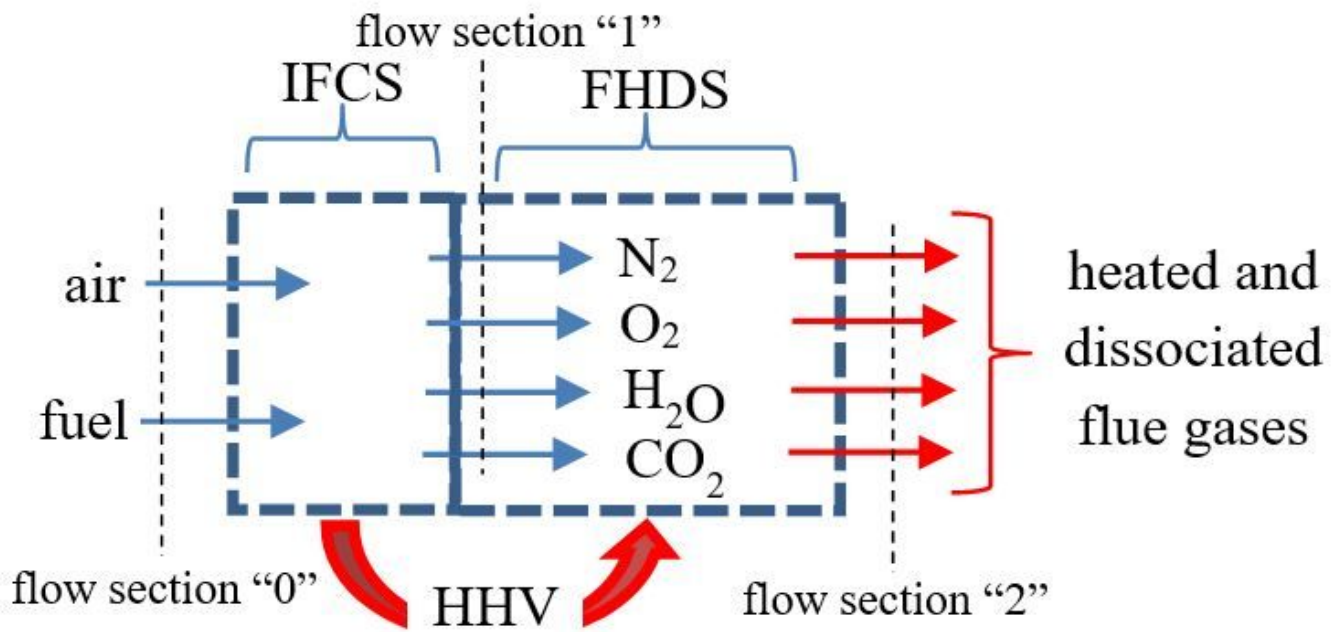


Figure 10

Please see the Manuscript PDF file for the complete figure caption.

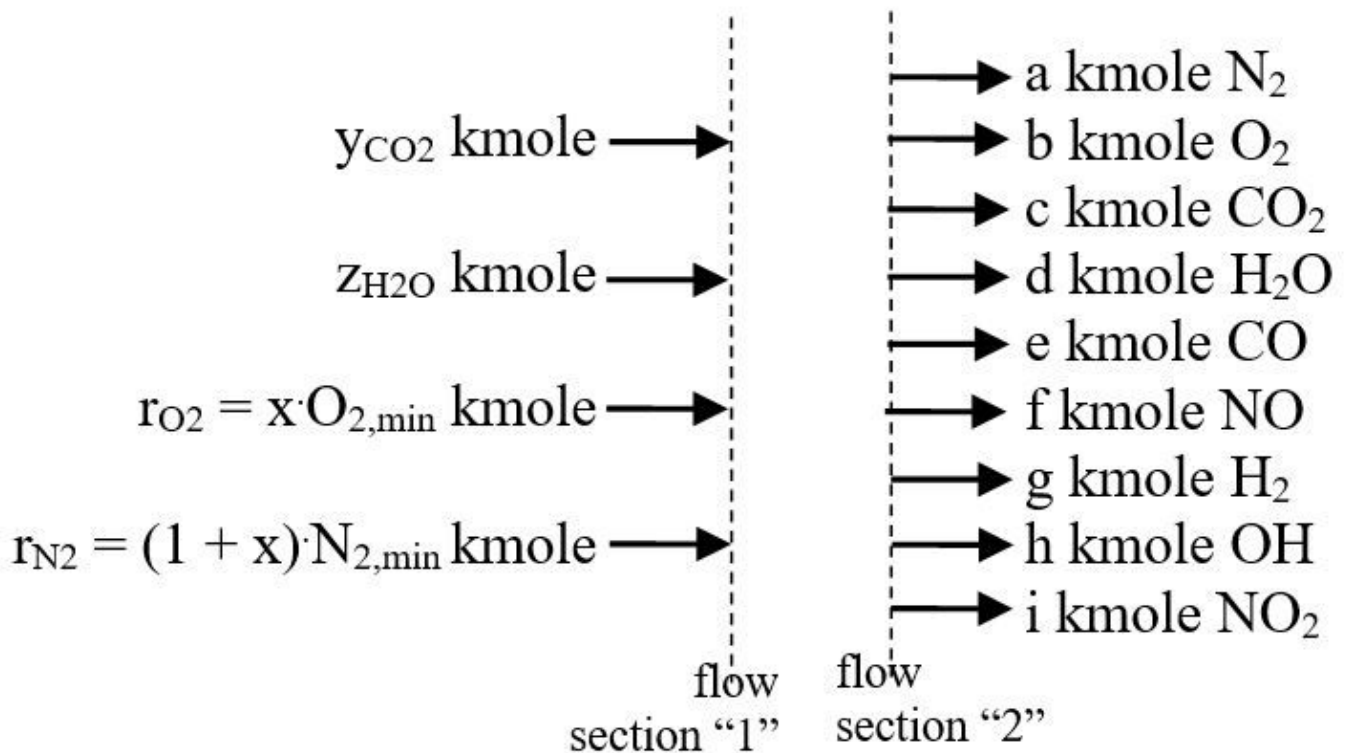


Figure 11

Please see the Manuscript PDF file for the complete figure caption.

Supplementary Files

This is a list of supplementary files associated with this preprint. Click to download.

- [Mat.supplimentary.docx](#)